Case Study

Volumetric Pothole Detection from UAV-Based Imagery

Siyuan Chen[1]; Debra F. Laefer, M.ASCE[2]; Xiangding Zeng[3]; Linh Truong-Hong, Ph.D.[4]; and Eleni Mangina[5]

Abstract: Road networks are essential elements of a community's infrastructure and need regular inspection. Present practice requires traffic interruptions and safety risks for inspectors. The road detection system based on vehicle-mounted lasers is also quite mature, offering advantages such as high-precision defect detection, high automation, and fast detection speed. However, it does have drawbacks such as high equipment procurement and maintenance costs, limited flexibility, and insufficient coverage range. Therefore, this paper proposes a low-cost unmanned aerial vehicle (UAV)-based alternative using imagery for automatic road pavement inspection focusing on pothole detection and classification. A slicing-based method, entitled the Pavement Pothole Detection Algorithm, is applied to the imagery after it is converted into a three-dimensional point cloud. When compared with manually extracted results, the proposed UAV-structure-from-motion (SfM) method and the associated algorithm achieved 0.01 m level accuracy for pothole depth detection and maximum errors of 0.0053 m^3 in volume evaluation for cases studies of both a road and a bridge deck. **DOI: 10.1061/JSUED2.SUENG-1458.**

Author keywords: Unmanned aerial vehicle (UAV); Photogrammetry; Structure from motion (SfM); Point cloud; Pavement evaluation.

Introduction

The safety of a community's road network is fundamental to an efficient transportation system and a functioning economy (Frisoni et al. 2014). Therefore, such networks must be inspected and maintained on a regular basis. In the US, road and bridge inspection and maintenance standards were developed largely following the collapse of the Silver Bridge in 1967. Specifically, in 1971, the National Bridge Inspection Standards (NBIS) were implemented as a result of the Federal-Aid Highway Act of 1968 (Schnebele et al. 2015). In Europe, the European Parliament Council on Road Infrastructure Safety Management issued European Directive 2008/96/EC as the legal basis for road safety inspection (Frisoni et al. 2014). In response, 4,852,242 km of road across 28 EU countries are monitored accompanied by 20 billion Euros in annual road maintenance (Nicodème et al. 2017).

At present, road damage detection is still mainly through manual detection, despite it being labor-intensive, time-consuming, subjective, requiring road closures, and putting inspectors in harms way (Varadharajan et al. 2014). For the road detection system based on a vehicle laser, which is not widely used, it has a great improvement in efficiency and detection accuracy compared with manual detection, and has strong application value. For example, the current mature commercial road detection system XROE XR-3D can achieve 4-m measurement coverage, and the absolute accuracy of the generated point cloud reaches the 0.01-m level. However, the vehicle-based radar road detection system usually faces difficulties in providing a full range of views and data for all parts of the road (including lanes, sidewalks, and slopes), the deployment flexibility is not enough to be limited by road traffic, and it is not safe and economical.

At present, some methods (Zeybek and Bicici 2020) based on structure from motion (SfM) use the SfM algorithm to generate point clouds from the road images and Global Mapper software to calculate the size of road pothole. These methods often have problems such as too much noise in the point cloud, incomplete pothole extraction, and large error in calculation of pothole size. Therefore, in order to overcome some of the shortcomings of the existing methods, the data acquisition stage and the damage treatment stage must achieve higher automation, cost effectiveness, and detection accuracy.

Related Works

With the development of new measurement sensors and data collection platforms, various technological solutions have been applied to detect and characterize pavement distress to plan pavement maintenance and repair tasks. An automated inspection effort typically consists of a two-stage data collection and analysis process. In both, there has been a general trend to evolve documentation and analysis from two-dimensional (2D) to more comprehensive three-dimensional (3D), and will be summarized in the following subsections.

Image-Based Two-Dimensional Inspection

As early as the 1990s, 2D images from satellites, airplanes, and road-based vehicles were employed for road pavement inspection (Chambon and Moliard 2011), along with accompanying data

[1]Associate Professor, School of Information Science and Engineering, Hunan Institute of Science and Technology, Yueyang 414000, China; School of Civil Engineering, Univ. College Dublin, Dublin, Ireland (corresponding author). Email: siyuan@hnist.edu.cn

[2]Professor, Center for Urban Science and Progress, Dept. of Civil and Urban Engineering, Tandon School for Engineering, New York, NY 10012; School of Civil Engineering, Univ. College Dublin, Dublin, Ireland. ORCID: https://orcid.org/0000-0001-5134-5322. Email: debra.laefer@nyu.edu

[3]College of Mechanical Engineering, Hunan Institute of Science and Technology, Yueyang 414000, China. Email: XiangdingZeng@vip.hnist.edu.cn

[4]School of Civil Engineering, Technical Univ. Delft, Delft 2628 CD, Netherlands. Email: l.truong@tudelft.nl

[5]Professor, School of Computer Science, Univ. College Dublin, Dublin D04C1P1, Ireland. ORCID: https://orcid.org/0000-0003-3374-0307. Email: Eleni.mangina@ucd.ie

Note. This manuscript was submitted on April 6, 2023; approved on October 19, 2023; published online on January 27, 2024. Discussion period open until June 27, 2024; separate discussions must be submitted for individual papers. This paper is part of the ***Journal of Surveying Engineering***, © ASCE, ISSN 0733-9453.

analysis methods. For example, Ma et al. (2013) identified geometric features for road damage segmentation from high-resolution satellite images. Subsequently, Coulibaly et al. (2015) adopted spectral and texture features to extract damaged road sections for postdisaster road inspection. With images captured from a moving vehicle, Varadharajan et al. (2014) proposed a method relying on superpixel and machine learning. In that study, texture, color, and geometric information were used for distress detection. More recently, Siriborvornratanakul (2018) proposed a method using single grayscale images and a 2D contour detection algorithm for pothole evaluation. However, in that case, the image were usually taken from a fixed view angle, and the analysis was affected by camera orientation and shadows. Notably, a single image of a scene can only provide 2D information, which contains insufficient information for depth evaluation or volume calculation.

Laser Scanning–Based Three-Dimensional Inspection

Over the last decade, aerial laser scanning (ALS), mobile laser scanning (MLS), and terrestrial laser scanning (TLS) have also been deployed for pavement inspection. In response, several researchers have undertaken automated damage detection algorithm development. For example, at the macroscale, Soilán et al. (2018) introduced a procedure to extract pavement and road markings from laser scanning point clouds based on an unsupervised learning method, and Vo et al. (2015a) used a fused imagery-ALS data set and a supervised machine learning approach for overall road extraction. At the microscale, Ouyang and Xu (2013) used a truck-mounted MLS for pavement cracking measurement. The achieved longitudinal resolution was 3 mm at a vehicle speed of 54 km/h. As part of that, a grid-based depth detection algorithm was designed for crack detection in the longitudinal and transverse directions, and the Haar transform (HT) was applied for edge detection of cracks by tracking the high-frequency depth changes. Subsequently, Gui et al. (2018) designed a frequency-based method for multidistress identification that included ruts, cracks, and grooves. This method was able to identify potholes and other damage from extremely high-resolution (1 million points/m^2) MLS point clouds.

Compared with traditional 2D, visual-based methods, and manual surveying methods, the 3D laser scanning–based methods demonstrated clear advantages in accuracy and comprehensiveness but have yet to be widely adopted in practice, possibly because of the cost of the laser scanners and the challenge in the management of large-scale data sets, which can rapidly reach the multiterabyte level (Laefer et al. 2017).

UAV-Photogrammetry Inspection and 3D Reconstruction

Both image-based and laser scanning–based inspection rely upon an acquisition platform (e.g., satellites, airplane, or on-road vehicle), and each platform has its own limitations in detecting ranges, fields of view, and vantage points. For example, an airplane can only collect from a distance between 1 and 20 km. Even high-end airborne LiDAR systems, when used with a helicopter at 3,000 m, typically have a spatial resolution no better than 0.1 m (Vo et al. 2015b), which is insufficient for small damage detection.

In recent years, developments in the fields of UAV design and computer vision have made the prospect of using a low-cost commercial UAV combined with a high-resolution digital camera a more viable strategy to meet the aforementioned challenges. UAV platforms in this context have many advantages. Foremost is economy. Specifically, according to a 2016 study on the popular commercial UAV platforms and on-board sensors, a quadrotor UAV equipped with a 4K (4096×2160 resolution) camera, and mechanical gimbal system in the price range of about $3,000 is available as a highly suitable platform for infrastructure inspections (Chen et al. 2016). An efficiency and cost comparison analysis by Tahar (2015) ranked UAV-based surveys as twice as fast and five times cheaper than traditional field survey methods (i.e., satellite imagery, airborne laser scanner, and crewed aircraft). Additionally, a UAV platform is more agile with respect to both inspection distance and view angles in ranges that cannot be provided by aircraft, satellite systems, or on-road vehicles.

Despite the numerous aforementioned advantages, UAVs still face certain limitations. For instance, in scenarios where tall trees or buildings are present along the route, it is often necessary to adjust the flight altitude based on the specific circumstances. Furthermore, there are restricted zones where flying is prohibited in certain specialized areas.

In some cases, UAV-based images have been used directly for visual inspection. For example, Eschmann et al. (2012) used UAVs for close-range building inspection and monitoring. In that work, images were collected from within meters of the building envelop for crack detection at the millimeter range. Seo et al. (2018) used UAV-based images for timber bridge inspection. They exploited multiple view angles for a bridge safety evaluation and compared the results with a standard Department of Transportation (DOT) manual inspection where spalling measurements were conducted at the centimeter level. They reported that multiple damage types (e.g., cracking, spalling, corrosion, and moisture) were detectable at levels equivalent to manual visual inspection. Pan et al. (2018) also applied UAV imagery in road inspection. By using the color information for feature extraction, potholes and cracks were automatically detected in 2D images. Machine learning algorithms including support vector machine (SVM), artificial neural networks, and random forest were then applied. Because of the 2D nature of the input data, although damage was reliably detected, volumetric quantification was not possible.

A more sophisticated solution using imagery involves the creation of a 3D reconstruction from 2D images. This derived 3D point cloud is then used for the damage evaluation. The most common method for generating the 3D reconstruction is structure from motion (SfM) (e.g., Micheletti et al. 2015; Bianco 2018; Azevedo et al. 2009). This method works by applying feature extraction and matching on multiple images taken from different perspective (the section "Related Works" provides a full description). Compared with traditional laser scanning, SfM-generated point clouds are economical because the data can be collected with any digital cameras, instead of heavier and more specialized equipment. When hosted on an UAV platform, data collection times and coverage rate can be highly controlled.

However, according to Caroti et al. (2015), output quality is highly related to data capturing strategies, the data collection instrument, and processing methodologies. Additionally, SfM-generated point clouds are generally less homogeneous and have more noise than those produced directly from laser scanners (Chen et al. 2019). Thus, identification and extraction of relatively small features (which would be representative of damage on the surface of infrastructure) has been especially challenging with UAV-SfM point clouds. A robust method has yet to be developed for 3D pavement damage detection and characterization from imagery data. This is the subject of this paper.

Research Scope and Methodology

This paper provides road pothole detection and volume loss estimation algorithm entitled the Pavement Pothole Detection (PPD)

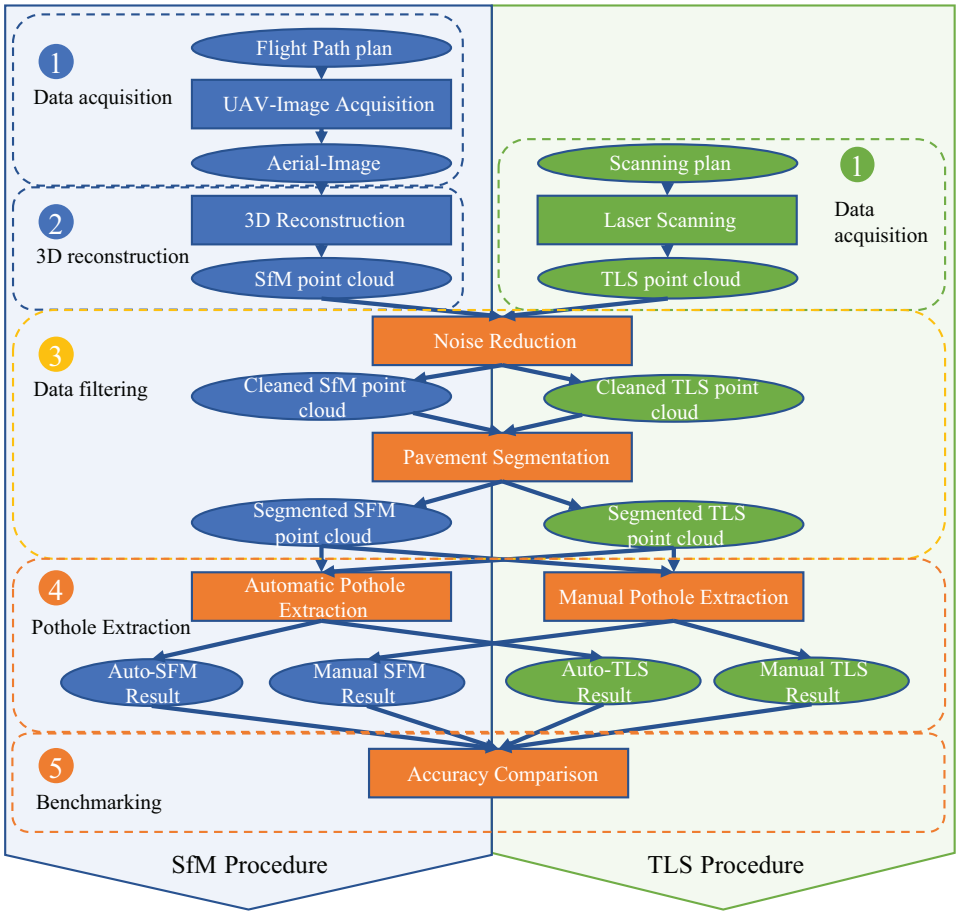

Fig. 1. (Color) Methodology for pothole detection and volume loss estimation.

algorithm. As shown in Fig. 1, the PPD workflow involves five steps: (1) data acquisition, (2) 3D reconstruction, (3) data filtering, (4) pothole extraction, and (5) benchmarking. Because Steps 1–3 employ existing techniques, they are only introduced briefly in this section.

Step 1: Data Acquisition

In a 2019 study, the impact of flight path, overlap rate, and flight altitude on the quality of point clouds generated by SfM was investigated (Chen et al. 2019). Specifically, bad camera positions will induce or aggravate problems like poor accuracy, incompleteness, and nonuniform data distribution. Using multiple parallel flight paths with an 80% overlap collected within 30 m of the road surface can minimize these effects.

Step 2: 3D Reconstruction

For the PPD algorithm, the 3D reconstruction procedure was achieved with a commonly used commercial SfM software package, Agisoft Photoscan (Agisoft version 1.11.4.0 build 5650). That software has three phases: (1) image alignment, (2) generation of a sparse 3D point cloud, and (3) generation of a dense 3D point cloud. To accelerate the alignment process, the Global Positioning System (GPS) information of each image was utilized, and the maximum key points number was limited to 40,000. The accuracy level and the dense reconstruction quality were set in the program as high.

Step 3: Data Filtering

A reconstructed point cloud typically contains significant outlier noise and redundant information, such as plants or obstacles around the road, which negatively impact the accuracy of further analysis. Therefore, a filtering procedure is required to (1) remove noise, and (2) segment the road section from the background environment. The first step is achieved herein by applying the statistical method to the point cloud (Chen et al. 2018). In this work, the commonly used statistical filter and geometry-based filter are compared. The Statistical Outlier Removal (SOR) filter was applied to calculate the average distance of each data point to its neighbors. In that process, a point will be marked as noise and removed if the distance to its closest neighbor exceeded the average distance derived from all points in the data set plus a standard deviation of that distance. The geometric-based filter takes into account the distance between a specific point and the surface of the object. The algorithm fits a plane locally through each point in the data set, utilizing neighboring points obtained either through a k-nearest neighbor (k-NN) search or a range search method.

Next, if the distance of the point to a fitting plane is larger than the threshold known as the max error rate (r), the point is considered as an outlier noise point. By comparing the false negatives of the two filtering algorithms [false positive rate (FPR) = number of normal points classified as noise/total normal points number], false positive [false negative rate (FNR) = number of noise classified as normal points/total noise points number] selects the statistical outlier removal with better effect (SOR) filter. This is represented by the following formula:

$$d_{\max} = \mu + \sigma \tag{1}$$

$$P_i, \ldots \text{if} \cdot \text{mean}|P_i - k\text{-NN}(P_i)| < d_{\max} \tag{2}$$

where μ = mean of the average distance of all points to the nearest point; σ = standard deviation of the average distance of all points to the nearest point; and k-NN = k-nearest neighbor algorithm, and the parameter set in this experiment is $k = 1$ (i.e., the nearest point).

Once the noise-removal step is completed, road segmentation occurs (Step 2). In that procedure, the cell-based region growing segmentation method introduced by Truong-Hong et al. (2018) was applied. That process uses a quadtree structure to separate the point cloud into small cells, after which the normal and residual value of each cell is compared with those of the neighboring cells. If the differences are smaller than the threshold, they are merged. The algorithm can adaptively select the growing conditions and parameters according to the characteristics of the actual point cloud data. For example, it can dynamically adjust the growing threshold according to the density, color, and other characteristics of the point cloud to achieve more accurate segmentation. In addition, by setting the growth conditions and restrictions, it can effectively suppress the growth of noise points so as to improve the accuracy and robustness of segmentation. In this way, the pavement surface is extracted for subsequent damage identification and extraction.

Step 4: Pothole Extraction

The first goal of this step is to identify road surface damage in the form of potholes. Areas are considered as potholes if the elevations of the section of the point cloud differs from the larger undamaged surface beyond a predesignated threshold. To identify those potholes, a 2D slicing method was designed to use a curve-fitting method to discriminate between damaged and undamaged areas. With the extracted damaged area, Delaunay triangulation was then applied to connect each point for volume calculation. Details of the procedure are described in Substeps A–F.

Substep A: Align the Point Cloud

The road was manually sliced as the input data, and a set of points $P = \{P1, P2, P3, \ldots, Pi, \ldots, Pm\} \in \mathbb{R}^3$ is stored with their x-y-z coordinates. To make the slicing procedure more efficient, singular value decomposition (SVD) has been applied to calculate the rotation matrix $\mathbf{V}$ to project the road section fit to the x-y plane, make the road extending along the x-axis, and the elevation along the z-direction, as shown in Fig. 2(a).

Substep B: 2D Slicing

To achieve the slicing, the data set was separated into multiple slices along the x-axis direction, as shown in Fig. 2(b). Each slice is a cross section of the road with a thickness of N, as was previously done by Zolanvari and Laefer (2016). To choose a proper N, a few points are randomly selected. For each point P_i, the distance to their nearest neighbor $P_{i'}$ are calculated using Eq. (3). Then, the average distance from point to point (d_{ave}) is calculated by Eq. (4). The term $N = 5 \times d_{\text{ave}}$ to ensure sufficient points in each slice for further curve fitting (the thickness N is derived empirically five times of d_{ave})

$$d_i = \sqrt{(x_{p_i} - x_{p_{i'}})^2 + (y_{p_i} - y_{p_{i'}})^2 + (z_{p_i} - z_{p_{i'}})^2} \tag{3}$$

$$d_{\text{ave}} = \frac{1}{n}\sum_{i=1}^{n} d_i \tag{4}$$

Substep C: 2D Curve Fitting

Within each slice of data, because the N is sufficiently small enough, each slice can be treated as a cross section in the y-z plane (Fig. 3). In this plane, a 2D polynomial curve can be generated to imitate the original undamaged surface. To eliminate the effect of damaged areas and the overfitting problem, the Random Sample Consensus (RANSAC) algorithm (Fischler and Bolles 1981) was applied. Points with a large displacement were marked as outlier points and ignored during the curve-fitting process.

Substep D: Neighborhood Adjustment

If damage dominates a slice, an overfitting problem will result. Specifically, the 2D curve would be fitted to the pothole profile instead of the undamaged surface. Because of that, a discontinuous border will exist between each slice, as shown in Fig. 4(a). To overcome this problem, the parameters of each fitting curve were adjusted with respect to their neighbor slices that are within the range of 1 m on each side of the slice under consideration. To achieve that, a moving median filter and a moving mean filter were applied on the polynomial parameters to remove the abnormal section and to smooth the boundaries. For any slice i, within a 1-m neighborhood, there are n intervals on each side. Each interval has its own fitted parameters P, after curve fitting. For section i, a new

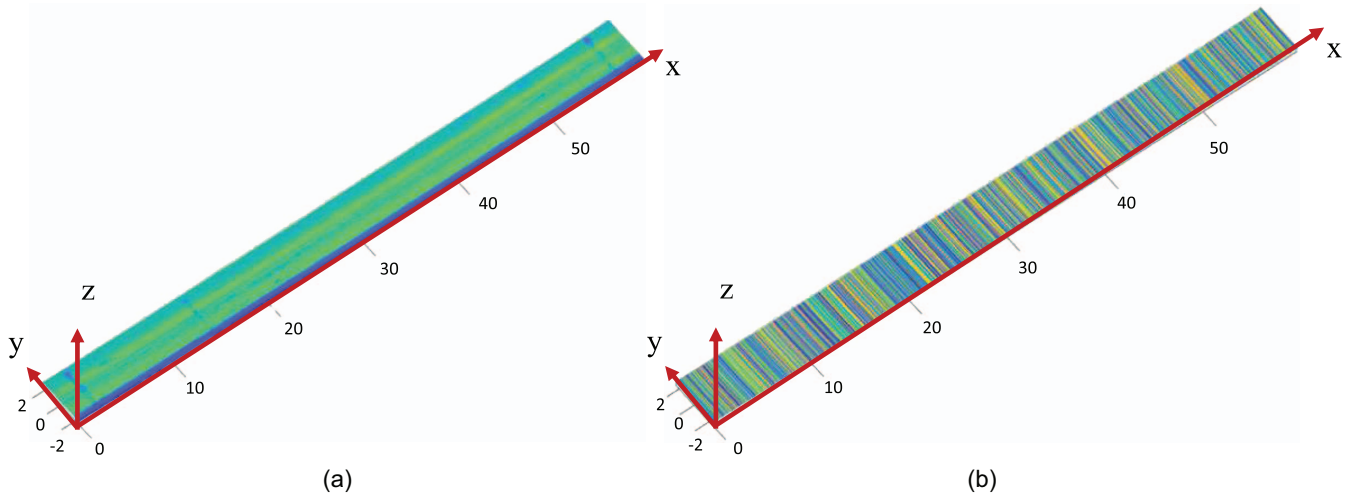

Fig. 2. (Color) Aligning and slicing process: (a) aligned point cloud in x-y plane; and (b) sliced point loud along x-direction.

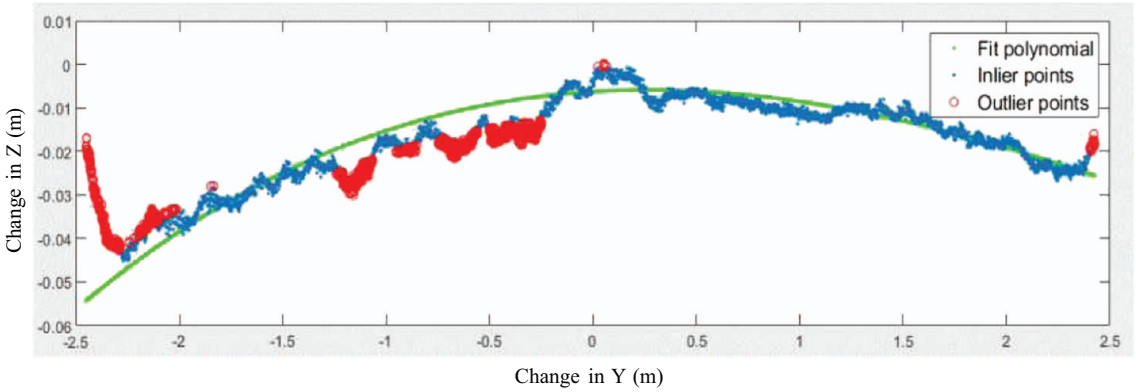

Fig. 3. (Color) Curve fitting in the y-z plane.

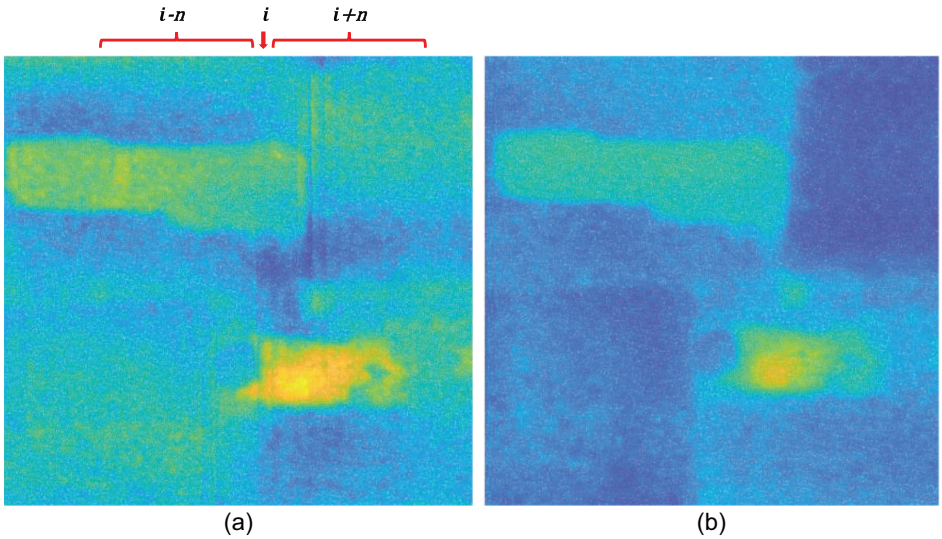

Fig. 4. (Color) Neighborhood adjustment: (a) discontinuous fitting; and (b) adjusted fitting.

parameter PM_i was assigned through Eq. (5) by calculating the median of all P values in the neighborhood. Similarly, through Eq. (6), the PA_i is calculated by computing the mean valve of the all PA_i in the neighborhood

$$PM_i = \text{median}\{P_{i-n}, \ldots, P_i, \ldots, P_{i+n}\} \tag{5}$$

$$PA_i = \text{mean}\{PM_{i-n}, \ldots, PM_i, \ldots, PM_{i+n}\} \tag{6}$$

After the application of the two filtering process, the adjusted results and parameter changes along the road longitudinal direction are shown in Figs. 4(b) and 5.

Substep E: Pothole Extraction

With the adjusted fitted curve in each slice, the residual distance δ_j of each point can be calculated [Eq. (7)]. The term δ_j is defined as the distance of each point from its own position Y_j to its projection position in the fitted curve $\hat{Y}_j$. Herein, for each point, if the residual is smaller than the selected threshold, those points will be marked as part of the regular surface. Choosing an appropriate threshold is an essential step in the PPD algorithm. Considering the road roughness, the mean value of the absolute residuals plus and minus two times of standard deviation are applied as the threshold. Points outside of this threshold are classified as defects [Eq. (8)]

$$\delta_j = \hat{Y}_j - Y_j \tag{7}$$

$$f(\delta_j) = \begin{cases} \text{if } \delta_j > \text{mean}(\delta_1, \ldots, \delta_j, \ldots, \delta_n) + 2 \times \text{std}(\delta_1, \ldots, \delta_j, \ldots, \delta_n): \text{Depression} \\ \text{else if } \delta_j < \text{mean}(\delta_1, \ldots, \delta_j, \ldots, \delta_n) - 2 \times \text{std}(\delta_1, \ldots, \delta_j, \ldots, \delta_n): \text{Projection} \\ \text{Otherwise: normal surface} \end{cases} \tag{8}$$

The classification is illustrated in Fig. 6.

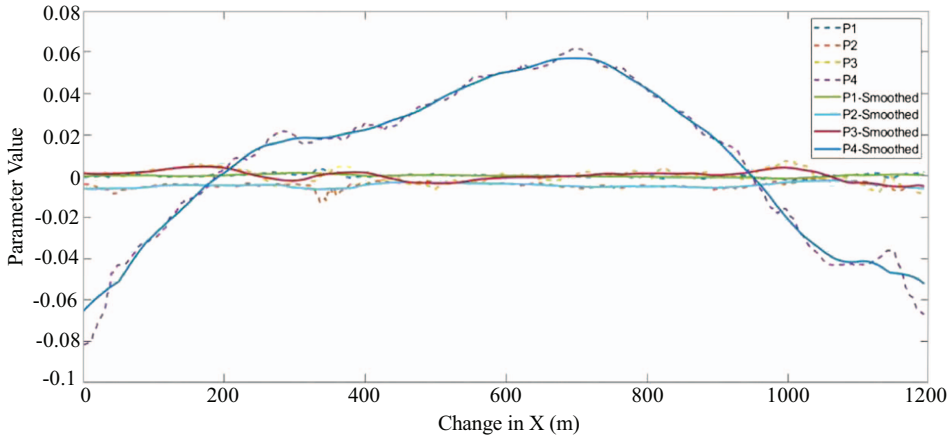

Fig. 5. (Color) Adjusting for polynomial curve parameters.

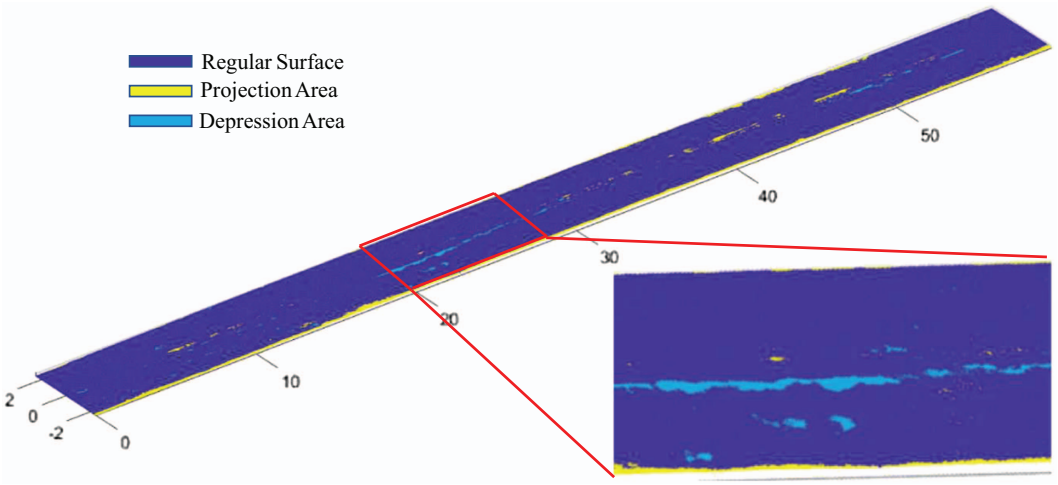

Fig. 6. (Color) Classification of the pavement.

Substep F: Mesh-Based Measurement

As shown in Fig. 7, by projecting the identified damage points P to the fitted curve, the group of points in the original surface could be restored (red points in the figure). That point set is noted as P_s, which represents the original undamaged surface. Therefore, the space enclosed by points P and P_s is the volume V_p missing inside the pothole. To calculate the value of V_p, a mesh is generated among the P and P_s points. The process is achieved by applying the built-in function AlphaShape in MATLAB software (Higham and Higham 2016). With this function, a mesh will be generated by the Delaunay triangulation method between points for volume and area calculation. The edge length is set as equal to or smaller than the maximum distance $d_i d_i$ from Substep B. An example is shown in Fig. 8. By setting a small volume threshold (e.g., 0.0005 m^3), noise, in the form of tiny holes caused by normal surface texture, can be removed. Similarly to 3D volume calculation, the area of the hole's missing surface could be calculated by applying an AlphaShape on projected points P_s.

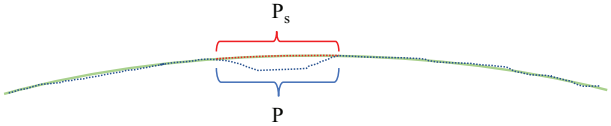

Fig. 7. (Color) Projection of undamaged surface.

Step 5: Benchmarking

To estimate the accuracy of the proposed UAV-SfM data capturing method and related damage-extraction algorithm, TLS data were collected for benchmarking. These data were collected with a Leica P20 Scan Station (Wetzlar, Germany) and postprocessed with Leica's proprietary software Cyclone (V9.1). Potholes were manually extracted from the TLS data as a reference set to compare the performance of the algorithm on both the TLS data set and UAV-SfM data set.

Field Trials

To benchmark the proposed PPD algorithm against a manual extraction from TLS data, two field trials were undertaken in Dublin, Ireland. The image collection process was conducted by a DJI Phantom 4 quadrotor (Shenzhen, China), equipped an independently controlled three-axis gimbal system and a digital camera

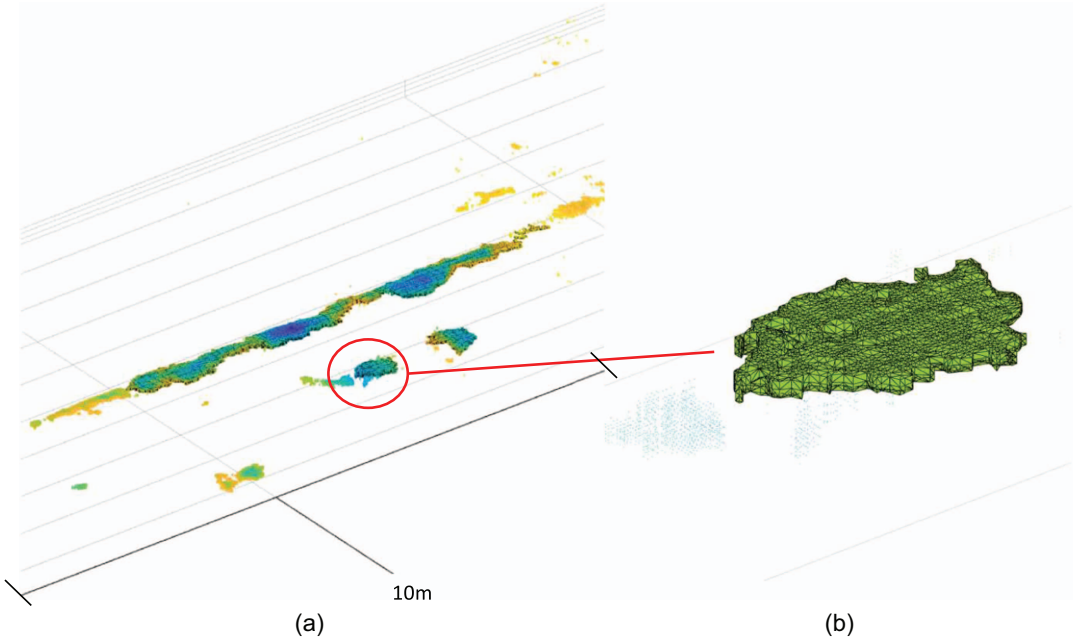

Fig. 8. (Color) (a) Mesh generation for volume and area measurement; and (b) close-up.

(12.4 million effective pixels). In accordance with Irish Aviation Authority regulations, flying was conducted manually by a trained operator with the help of on-board GPS and obstacle detection sensors.

Field Trial 1: UCD Road

Field trial 1 was for a 140-m-long by 5-m-wide asphalt road section at the University College Dublin (UCD) campus. The road was partially covered by tree canopy (near left and far right in Fig. 9), which caused shadows and obstructed the fight path at some points, and it had evidence of a few previous repairs (Fig. 10). There were no prominent obstacles (such as rocks, tree branches, and so on) on this stretch of road. The primary concern is to identify road damage. In future research, our focus will be on addressing the challenge of distinguishing between road obstacles and road damage.

Fig. 9. (Color) Leica P20 Scan Station at the data collection site.

A pair of UAV flights was undertaken. Depending upon the presence of trees, the first was 8–10 m above the ground and collected 58 aerial images. The second was 20 m and collected 39 images. All 97 images were used as input for the 3D reconstruction. A point cloud of 57 million points was generated. Accompanying this was the TLS data set, which was comprised of about 34 million points collected in 20 min from five scan stations from single side of the road. The resolution setting was 6.3 mm at 10 m. In this data set, three potholes (I–III) were manually extracted, as shown in Fig. 11.

Field Trial 2: Wicklow Bridge Deck

The second field trial was of an asphalt bridge deck located in County Wicklow in south Dublin. At this site, there were no obstacles around the bridge and no objects casting shadows. At 150 m long and 4.8 m wide, the pavement size was similar to that in Field trial 1. The Field trial 1 flight path was repeated, resulting in 91 aerial images in 12 min (60 from 10 m above and 31 from 20 m above). A total of 4 images containing vehicles were manually removed. The remaining 87 images were used as the input for the 3D reconstruction, resulting in a point cloud of 43 million points. The accompanying TLS data set had 270 million points and was collected in 180 min from 10 scan stations. The resolution setting was 5 mm at 10 m. From both data sets, six potholes were manually extracted (shown as B-I to B-VI in Fig. 12).

Results and Error Source Analysis

Automatic pothole extraction was applied in both the SfM and TLS point clouds. The manual extraction results of each data set are also presented (Tables 1–6 and Fig. 13). By comparing each result with the average result, the maximum discrepancy in the two data sets was found to occur in Pothole A-III in the UCD road study. A possible reason is that previous repairs posed a challenge for the curve fitting because the final road surface was neither flat nor sloped in a consistent manner. Specifically, Fig. 14 shows the three repaired patches (marked with A, B, and C) causing a different and uneven

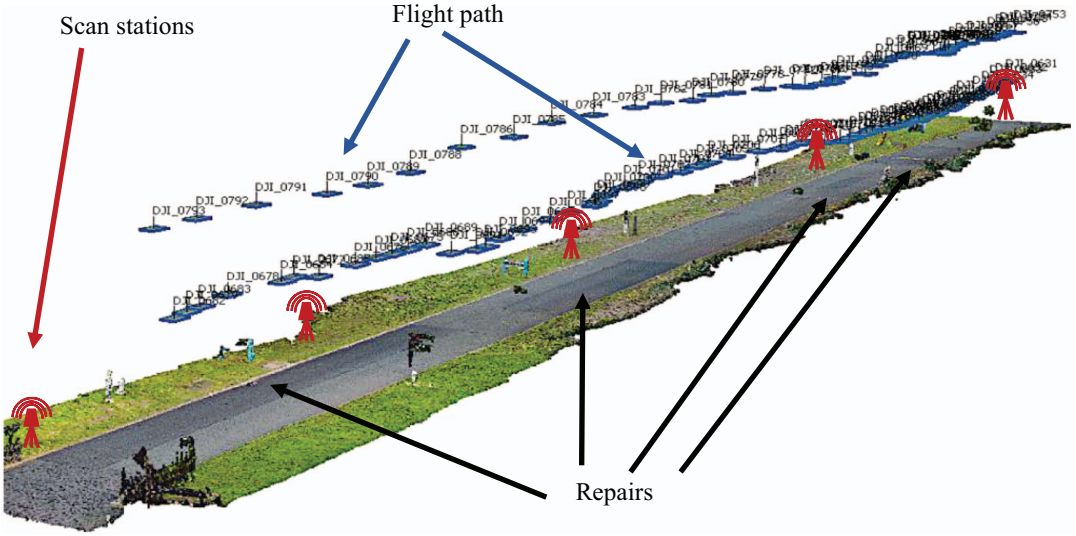

Fig. 10. (Color) Flight path and scanner arrangement.

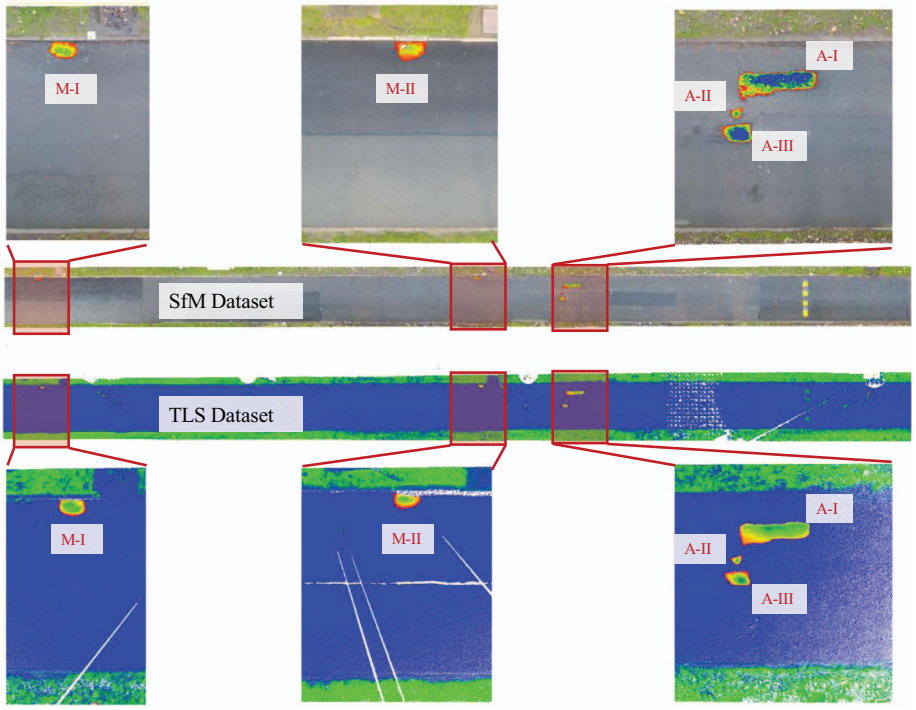

Fig. 11. (Color) Manually extracted potholes in UCD data sets (damage shown in red squares).

elevation compared with the original road surface. These factors affected the surface fitting process, and the accuracy of the extraction process, irrespective of whether the extraction was automatic or manual.

In the automatic extraction process, the algorithm use the repaired patches as the original surface, even though they had a higher elevation. Thus, over extraction issues happened, with more points that did not belong to the potholes being extracted. During the manual extraction process, the lower unrepaired surface was considered as the original surface. This difference caused the errors, though the neighborhood adjustment process minimized the situation. As a result, at Pothole A-III, the maximum volume difference was 31% (0.3802 m^2) from the TLS autoextraction result, the area difference was 25% (0.1352 m^2), and the depth difference was 38% (0.0187 m). Except for that area, most volume detection errors did not exceed the millimeter level (±30%), and the automatic method had relatively smaller errors for most of the potholes.

Discussion

In this automatic pothole inspection pipeline, both TLS and SfM data sets were tested, and potholes were readily identified in each approach. Arguably, the SfM data sets had advantages

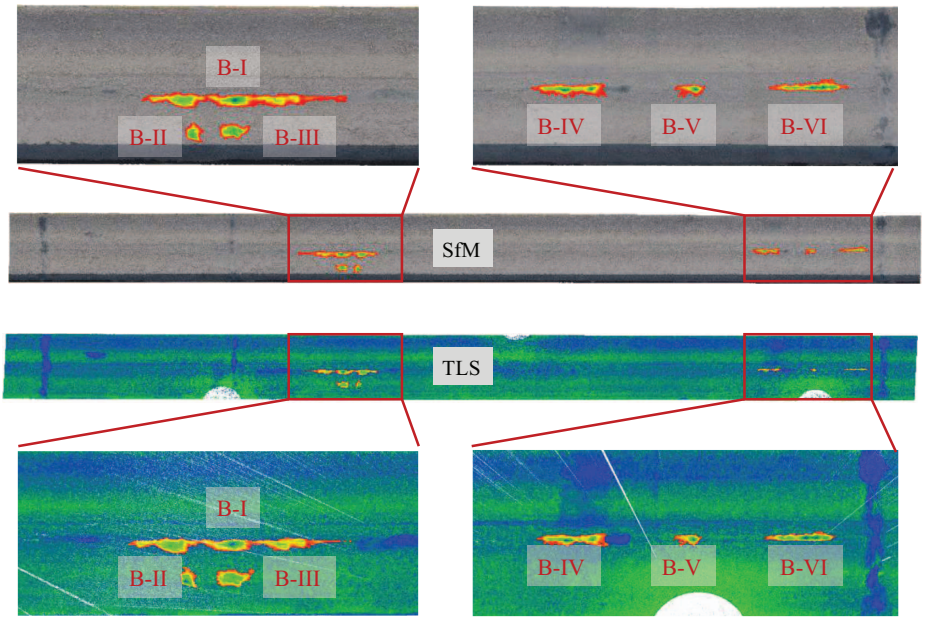

Fig. 12. (Color) Location of target potholes in SfM and TLS bridge data sets.

Table 1. Volume comparison (cm^3)

Pothole No.	SfM-Auto	TLS-Auto	SfM-Manual	TLS-Manual	Mean
A-I	25,686	27,869	24,888	26,036	26,120
A-II	938	1,109	535	780	841
A-III	14,137	15,712	9,068	8,801	11,929
B-I	20,315	18,080	19,825	17,448	18,917
B-II	2,392	1,609	1,821	2,134	1,989
B-III	4,150	3,149	4,497	5,006	4,200
B-IV	5,394	3,260	4,810	4,396	4,465
B-V	925	1,055	901	1,384	1,066
B-VI	2,065	2,500	2,432	2,434	2,358

Table 2. Volume errors

	SfM-Auto		TLS-Auto		SfM-Manual		TLS-Manual	
Pothole No.	Volume error (cm^3)	Percentage	Volume error (cm^3)	Percentage	Volume error (cm^3)	Percentage	Volume error (cm^3)	Percentage
A-I	−434	−2	1,749	7	−1,232	−5	−84	0
A-II	97	12	269	32	−306	−36	−60	−7
A-III	1,970	16	3,545	29	−1,713	−14	−3,802	−31
B-I	1,398	7	−837	−4	908	5	−1,469	−8
B-II	403	20	−380	−19	−168	−8	145	7
B-III	−50	−1	−1,052	−25	296	7	806	19
B-IV	929	21	−1,205	−27	345	8	−69	−2
B-V	−141	−13	−11	−1	−165	−16	318	30
B-VI	−292	−12	142	6	74	3	76	3

during processing. The color information in the SfM data sets is better presented than TLS data set (Fig. 15). The color assists in manual extraction, but also could be used as a feature in an autosegmentation process. Conversely, the TLS data can provide intensity information, which is not available from a UAV-SfM data set and has been used for material classification in some studies (Andrews et al. 2013).

Another advantage of the SfM data sets are their relatively uniform densities, achieved by the UAV images being collected from multiple well-distributed viewpoints. Conversely, the TLS data

Table 3. Area comparison (cm^2)

Pothole No.	SfM-Auto	TLS-Auto	SfM-Manual	TLS-Manual	Mean
A-I	10,992	11,613	11,368	11,153	11,281
A-II	529	644	579	794	636
A-III	6,025	6,093	4,904	5,258	5,570
B-I	11,139	11,394	12,621	11,268	11,605
B-II	1,274	1,145	748	940	1,027
B-III	2,176	2,026	2,306	2,984	2,373
B-IV	3,383	3,299	5,056	4,616	4,088
B-V	764	1,039	711	833	837
B-VI	2,798	2,357	2,289	1,691	2,284

Table 4. Area errors

	SfM-Auto		TLS-Auto		SfM-Manual		TLS-Manual	
Pothole No.	Area error (cm^2)	Percentage	Area error (cm^2)	Percentage	Area error (cm^2)	Percentage	Area error (cm^2)	Percentage
A-I	−290	−3	331	3	87	1	−128	−1
A-II	−108	−17	8	1	−57	−9	157	25
A-III	548	10	616	11	189	3	−1,352	−25
B-I	−467	−4	−211	−2	1,016	9	−337	−3
B-II	247	24	118	12	−279	−27	−87	−8
B-III	−197	−8	−347	−15	−67	−3	611	26
B-IV	−705	−17	−790	−19	968	24	527	13
B-V	−73	−9	202	24	−126	−15	−4	0
B-VI	514	23	73	3	6	0	−593	−26

Table 5. Maximum height comparison (cm)

Pothole No.	SfM-Auto	TLS-Auto	SfM-Manual	TLS-Manual	Mean
A-I	2.64	2.94	2.55	3.10	2.81
A-II	2.39	2.81	1.62	1.92	2.19
A-III	5.28	5.32	4.32	3.75	4.67
B-I	3.84	3.28	3.68	3.26	3.51
B-II	2.49	2.27	2.70	2.60	2.51
B-III	2.32	2.42	2.69	2.89	2.58
B-IV	2.54	2.76	2.42	2.77	2.62
B-V	2.24	2.79	2.33	2.78	2.54
B-VI	2.48	2.24	1.87	2.07	2.16

Table 6. Maximum height errors

	SfM-Auto		TLS-Auto		SfM-Manual		TLS-Manual	
Pothole No.	Height error (cm)	Percentage	Height error (cm)	Percentage	Height error (cm)	Percentage	Height error (cm)	Percentage
A-I	−0.17	−6	0.14	5	−0.26	−9	0.29	10
A-II	0.21	10	0.62	28	−0.57	−26	−0.27	−12
A-III	0.34	7	0.38	8	1.15	23	−1.87	−38
B-I	0.32	9	−0.23	−7	0.17	5	−0.25	−7
B-II	−0.02	−1	−0.25	−10	0.19	7	0.09	3
B-III	−0.26	−10	−0.16	−6	0.11	4	0.31	12
B-IV	−0.08	−3	0.14	5	−0.20	−8	0.15	6
B-V	−0.29	−12	0.26	10	−0.21	−8	0.24	10
B-VI	0.32	15	0.07	3	−0.29	−14	−0.09	−4

Fig. 13. (Color) Error analysis.

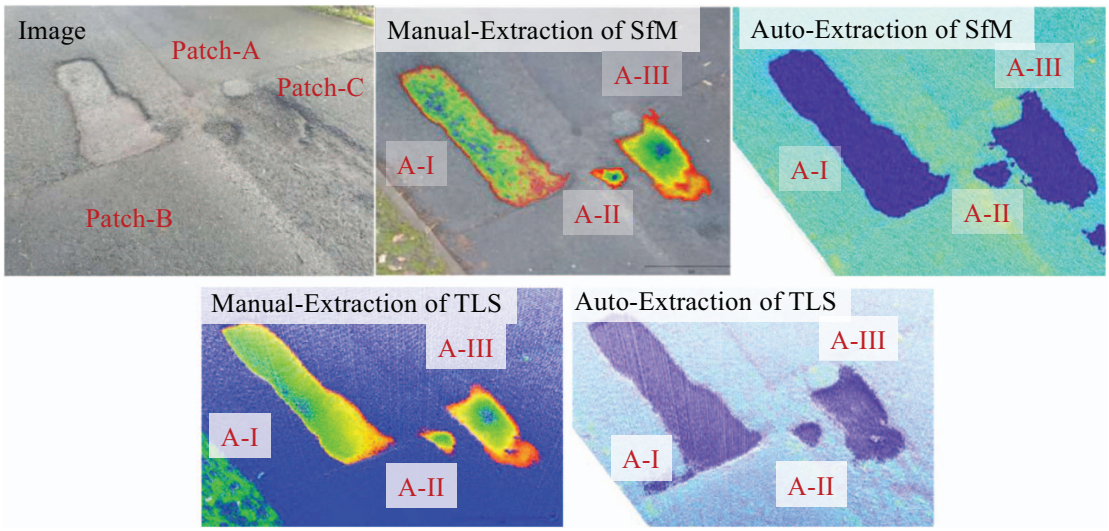

Fig. 14. (Color) Visual check of inspection results.

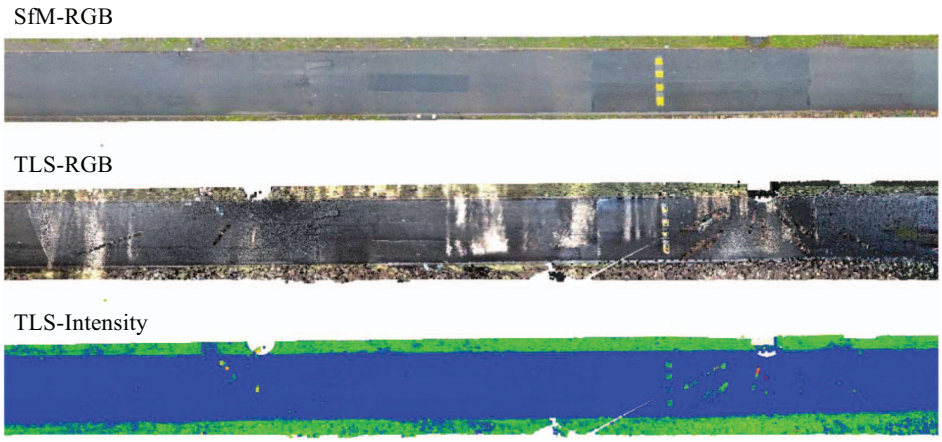

Fig. 15. (Color) Visual comparison of SfM and TLS data sets.

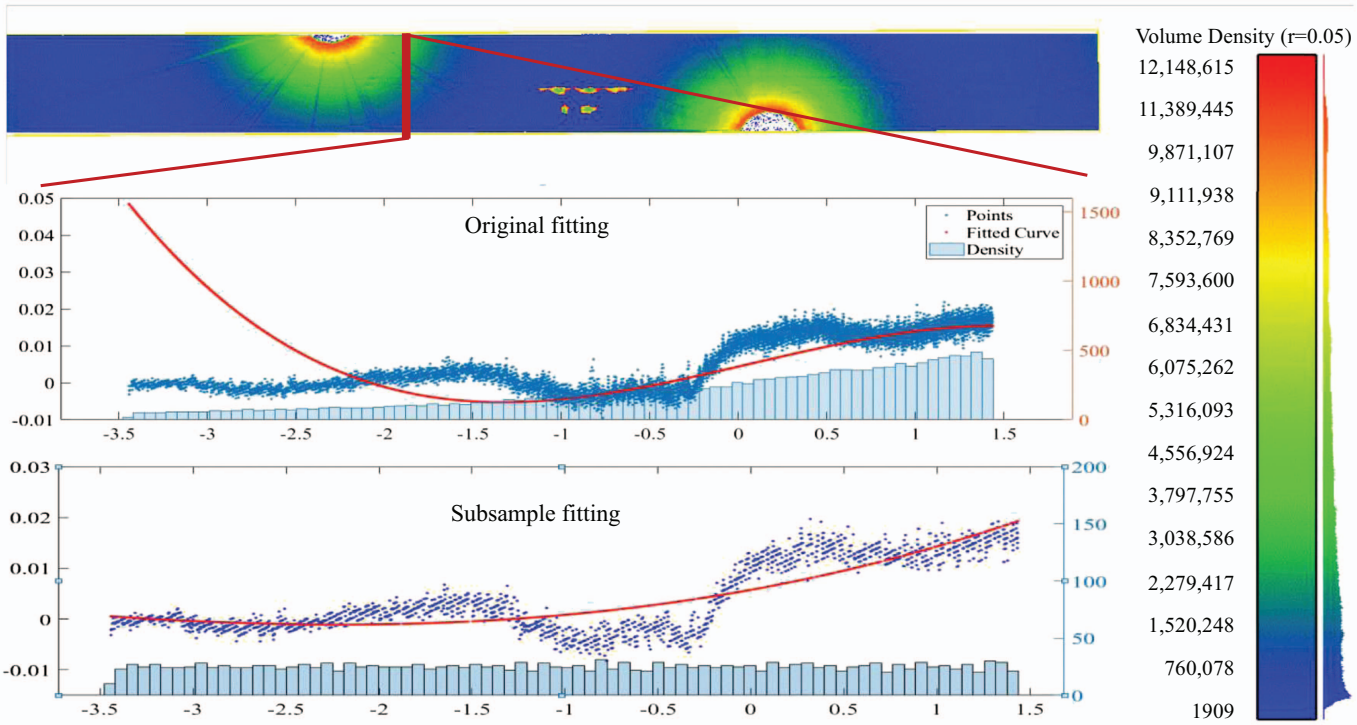

Fig. 16. (Color) Effect of nonuniform distribution.

sets have serious radial distribution biases. Thus, data collection from one side of the road have much denser points than the other side, which introduces errors in the curve-fitting process proposed herein. For the cross section shown in Fig. 16, the fitted curve will be skewed to the right side surface, whereas points on the left will be ignored due to the much higher density on the right. In this case, it causes a problem for the pothole extraction in TLS data set. Additionally, due to the points density drops and radial distribution, the TLS data set contains some empty gaps, which look like white strips (Fig. 17). The missing points along these strips will cause subsequent problems for detailed extraction and mesh generation. The SfM data set does not have this kind of problem.

Although MLS would arguably have been a more competitive technology against which to benchmark the SfM method, such equipment was not available. Thus, only TLS data were compared in this study. Instead of surveying a site with a static scanner, the MLS can inherently capture data from multiple viewpoints, which can significantly reduce the nonuniform density problem.

Conclusions

As a supplement to traditional road inspection methods, this work proposed a novel workflow using UAV images and a 3D reconstruction method for road inspection (currently applied in the most extensive range of ordinary roads, excluding special sections such as transition curves and superelevated roads). The main steps are image acquisition, 3D reconstruction, noise reduction, and damage extraction. Focusing on damage extraction, an automatic pothole detection and evaluation algorithm has been proposed.

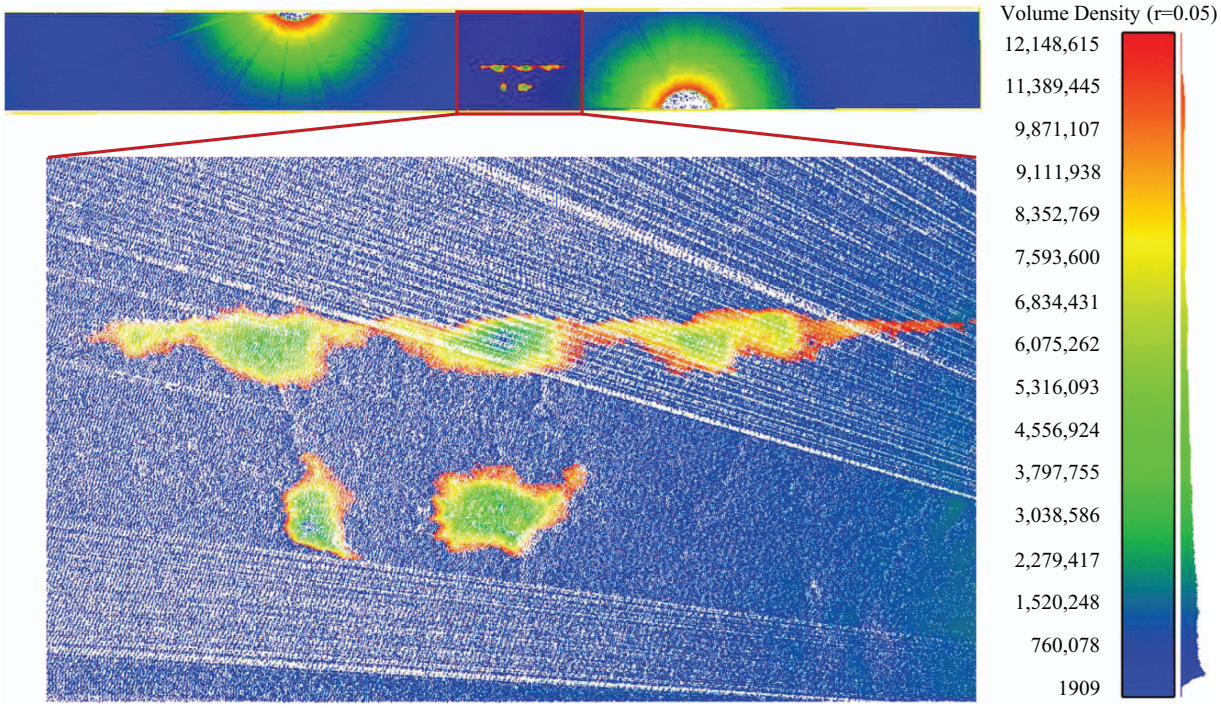

Fig. 17. (Color) Strip gaps in the TLS data sets.

Using a slicing method and 2D curve-fitting tool, this algorithm could extract potholes and calculate related geometric information, such as volume, area, and depth.

To evaluate the accuracy of the data acquisition method and the extraction algorithm, case studies have been conducted in UCD Road and Wicklow Bridge. These proved that the proposed inspection method could successfully detect all potholes and extract the contour. For the geometry evaluation, the depth evaluation errors were less than 0.0034 m when comparing the autoextraction result with manual extraction results. In the last, when comparing the UAV-SfM points with the TLS point cloud, some advantages included more uniform density distribution and better color rendition.

Overall, this study has primary explored the new direction of using UAV for road evaluation. As a relatively new method, the validation of this approach for engineering inspection is still in its infancy and faces both technical and cultural challenges prior to widespread adoption being likely. In the future, with the development of more advanced algorithms, the accuracy of the UAV-SfM method for road inspection could be further improved.

Data Availability Statement

All data and code that support the findings of this study are available from the corresponding author upon reasonable request.

Acknowledgments

This project was made possible through the generous support of the European Union's Horizon 2020 Research and Innovation programme, Marie Skłodowska-Curie Grant No. 642453. This work was supported by Research on Road Detection Method Based on UAV Image Reconstruction Technology (Item No. 20B266); Research on Monitoring Technology and Application of Bank Collapse Based on 3D Reconstruction (Item No. XSKJ2021000-13); and Research and Application of Efficient Road and Crack Defect Detection (Item No. 211076656073).

Author contributions: Siyuan Chen: formulation or evolution of overarching research goals and aims and supervision. Debra F. Laefer: writing–original draft and resources. Xiangding Zeng: writing–review and editing. Linh Truong-Hong: data curation. Eleni Mangina: formal analysis.

References

Andrews, D. P., J. Bedford, and P. G. Bryan. 2013. "A comparison of laser scanning and structure from motion as applied to the great barn at Harmondsworth, UK." *Int. Arch. Photogramm. Remote Sens. Spatial Inf. Sci.* 5 (Jul): W2. https://doi.org/10.5194/isprsarchives-XL-5-W2-31-2013.

Azevedo, T., J. Tavares, and M. Vaz. 2009. "3D object reconstruction from uncalibrated images using an off-the-shelf camera." In *Vision and medical image*. Berlin: Springer.

Bianco, S. 2018. "Evaluating the performance of structure from motion pipelines." *J. Imaging* 4 (8): 98. https://doi.org/10.3390/jimaging4080098.

Caroti, G., I. Martínez-Espejo Zaragoza, and A. Piemonte. 2015. "Accuracy assessment in structure from motion 3D reconstruction from UAV-born images: The influence of the data processing methods." *ISPRS Arch.* 40 (Mar): 103–109. https://doi.org/10.5194/isprsarchives-XL-1-W4-103-2015.

Chambon, S., and J.-M. Moliard. 2011. "Automatic road pavement assessment with image processing: Review and comparison." *Int. J. Geophys.* 2011 (Nov): 1–20. https://doi.org/10.1155/2011/989354.

Chen, S., D. F. Laefer, and E. Mangina. 2016. "State of technology review of civilian UAVs." *Recent Pat. Eng.* 10 (Nov): 160–174. https://doi.org/10.2174/1872212110666160712230039.

Chen, S., D. F. Laefer, E. Mangina, S. M. I. Zolanvari, and J. Byrne. 2019. "UAV bridge inspection through evaluated 3D reconstructions." *J. Bridge Eng.* 24 (4): 05019001. https://doi.org/10.1061/(ASCE)BE.1943-5592.0001343.

Chen, S., L. Truong-hong, E. O. Keeffe, D. F. Laefer, and E. Mangina. 2018. "Outlier detection of point clouds generating from low cost UAVs

for bridge inspection, in." In *Proc., 6th Int. Symp. on Life-Cycle Civil Engineering*, 1969–1975. London: Taylor & Francis.
Coulibaly, I., R. Lepage, and M. Saint-Jacques. 2015. "Road damage detection from high resolution satellite images based on machine learning." In *MultiTemp 2015*, 1–5. New York: IEEE.
Eschmann, C., C.-M. Kuo, and C. Boller. 2012. "Unmanned aircraft systems for remote building inspection and monitoring." In *Proc., 6th European Workshop on Structural Health Monitoring*, 1–8. Dresden, Germany: RWTH Publications.
Fischler, M. A., and R. C. Bolles. 1981. "Random sample consensus: A paradigm for model fitting with applications to image analysis and automated cartography." *Commun. ACM* 24 (Mar): 381–395. https://doi.org/10.1145/358669.358692.
Frisoni, R., F. Dionori, L. Casullo, C. Vollath, L. Devenish, F. Spano, T. Sawicki, and S. Carl. 2014. *EU road surfaces: Economic and safety impact of the lack of regular road maintenance*. Brussel, Belgium: European Parliament Library.
Gui, R., X. Xu, D. Zhang, H. Lin, F. Pu, L. He, and M. Cao. 2018. "A component decomposition model for 3D laser scanning pavement data based on high-pass filtering and sparse analysis." *Sensors* 18 (7): 2294. https://doi.org/10.3390/s18072294.
Higham, D. J., and N. J. Higham. 2016. *MATLAB guide society for industrial and applied mathematics*. Philadelphia: SIAM Publications Library.
Laefer, D. F., S. Abuwarda, A.-V. Vo, L. Truong-Hong, and H. Gharibi. 2017. *2015 aerial laser and photogrammetry survey of Dublin city collection record*, 1–8. New York: New York Univ.
Ma, H., N. Lu, L. Ge, Q. Li, X. You, X. Li, N. Earthquake, and I. Service. 2013. "Automatic road damage detection using high-resolution satellite images and road maps." In *Proc., Geoscience and Remote Sensing Symp. (IGARSS)*, 3718–3721. New York: IEEE.
Micheletti, N., J. H. Chandler, and S. N. Lane. 2015. "Structure from motion (SfM) photogrammetry." In *British Society for Geomorphology geomorphological techniques*, 1–12. London: British Society of Geomorphology.
Nicodème, C., K. Diamandouros, J. Diez, C. Durso, K. Arampidou, and A. K. Nuri. 2017. *Road statistics year book*. Washington, DC: Transportation Research Board.
Ouyang, W., and B. Xu. 2013. "Pavement cracking measurements using 3D laser-scan images." *Meas. Sci. Technol.* 24 (2013): 1–9. https://doi.org/10.1088/0957-0233/24/10/105204.
Pan, Y., X. Zhang, G. Cervone, and L. Yang. 2018. "Detection of asphalt pavement potholes and cracks based on the unmanned aerial vehicle multispectral imagery." *IEEE J. Sel. Top. Appl. Earth Obs. Remote Sens.* 11 (Sep): 3701–3712. https://doi.org/10.1109/JSTARS.2018.2865528.
Schnebele, E., B. F. Tanyu, G. Cervone, and N. Waters. 2015. "Review of remote sensing methodologies for pavement management and assessment." *Eur. Transp. Res. Rev.* 7 (May): 7. https://doi.org/10.1007/s12544-015-0156-6.
Seo, J., L. Duque, and J. Wacker. 2018. "Drone-enabled bridge inspection methodology and application." *Autom. Constr.* 94 (May): 112–126. https://doi.org/10.1016/j.autcon.2018.06.006.
Siriborvornratanakul, T. 2018. "An Automatic road distress visual inspection system using an onboard in-car camera." *Adv. Multimedia* 2018 (Jun): 1–10. https://doi.org/doi.org/10.1155/2018/2561953.
Soilán, M., L. Truong-Hong, B. Riveiro, and D. Laefer. 2018. "Automatic extraction of road features in urban environments using dense ALS data." *Int. J. Appl. Earth Obs. Geoinf.* 64 (May): 226–236. https://doi.org/10.1016/j.jag.2017.09.010.
Tahar, K. N. 2015. "Efficiency and cost comparison of UAV/Field survey." In *Proc., 2015 Int. Conf. on Space Science and Communication (IconSpace)*, 428–433. New York: IEEE.
Truong-Hong, L., S. Chen, V. L. Cao, and D. F. Laefer. 2018. "Automatic bridge deck damage using low cost UAV-based images." In *TU1406 quality specifications for roadway bridges standardization at a European level*, 1–6. Brussels, Belgium: European Cooperation in Science and Technology.
Varadharajan, S., S. Jose, K. Sharma, L. Wander, and C. Mertz. 2014. "Vision for road inspection." In Vol. 2014 of *Proc., 2014 IEEE Winter Conf. on Applications of Computer Vision, WACV*, 115–122. New York: IEEE.
Vo, A. V., L. Truong-Hong, and D. F. Laefer. 2015a. "Aerial laser scanning and imagery data fusion for road detection in city scale." In *Proc., Int. Geoscience and Remote Sensing Symp. (IGARSS)*, 4177–4180. New York: IEEE.
Vo, A. V., L. Truong-Hong, D. F. Laefer, D. Tiede, S. D'Oleire-Oltmanns, A. Baraldi, M. Shimoni, G. Moser, and D. Tuia. 2015b. "Processing of extremely high resolution LiDAR and RGB Data: Outcome of the 2015 IEEE GRSS data fusion contest—Part B: 3-D contest." *IEEE J. Sel. Top. Appl. Earth Obs. Remote Sens.* 12 (Mar): 5560–5575. https://doi.org/10.1109/JSTARS.2016.2581843.
Zeybek, M., and S. Biçici. 2020. "Road distress measurements using UAV." *Turkish J. Remote Sens. GIS* 1 (1): 13–23.
Zolanvari, S. I., and D. F. Laefer. 2016. "Slicing method for curved façade and window extraction from point clouds." *ISPRS J. Photogramm. Remote Sens.* 119 (Sep): 334–346. https://doi.org/10.1016/j.isprsjprs.2016.06.011.